Available online at www.sciencedirect.com

ScienceDirect

journal homepage: www.elsevier.com/locate/he

Ternary transition metal alloy FeCoNi nanoparticles on graphene as new catalyst for hydrogen sorption in MgH_2

Sweta Singh [b], *Ashish Bhatnagar* [c], *Vivek Shukla* [a], *Alok K. Vishwakarma* [a], *Pawan K. Soni* [a], *Satish K. Verma* [a], *M.A. Shaz* [a], *A.S.K. Sinha* [d], *O.N. Srivastava* [a,*]

[a] *Hydrogen Energy Centre, Department of Physics, Banaras Hindu University, Varanasi 221005, U.P, India*
[b] *Department of Physics, Mahatma Gandhi Central University, Motihari, 845401, Bihar, India*
[c] *Department of Physics and Materials Science and Engineering, Jaypee Institute of Information Technology, Noida, 201309, India*
[d] *Department of Chemical Engineering and Technology, Indian Institute of Technology, Banaras Hindu University, Varanasi, 221005, India*

HIGHLIGHTS

- Synthesis of FeCoNi@GS by one pot method.
- FeCoNi@GS has been used as catalyst for MgH_2.
- MgH_2 catalyzed by FeCoNi@GS show excellent cyclability.
- Formation enthalpy of MgH_2: FeCoNi@GS is reduced by 19.26 kJ/mol of H_2 as compared to ball milled MgH_2.

GRAPHICAL ABSTRACT

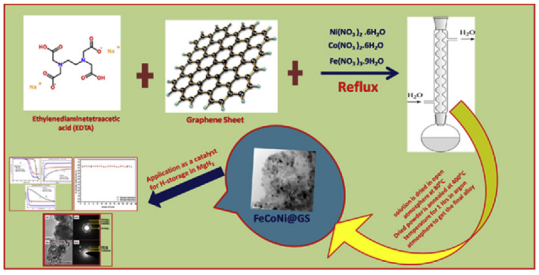

ARTICLE INFO

Article history:
Received 26 June 2019
Received in revised form
22 September 2019
Accepted 25 October 2019
Available online 18 November 2019

Keywords:
Ternary alloy FeCoNi
Graphene templated FeCoNi
MgH_2
Hydrogen storage

ABSTRACT

The present investigation deals with the synthesis of ternary transition metal alloy nanoparticles of FeCoNi and graphene templated FeCoNi (FeCoNi@GS) by one-pot reflux method and there use as a catalyst for hydrogen sorption in MgH_2. It has been found that the MgH_2 catalyzed by FeCoNi@GS (MgH_2: FeCoNi@GS) has the onset desorption temperature of ~255 °C which is 25 °C and 100 °C lower than MgH_2 catalyzed by FeCoNi (MgH_2: FeCoNi) (onset desorption temperature 280 °C) and the ball-milled (B.M) MgH_2 (onset desorption temperature 355 °C) respectively. Also MgH_2: FeCoNi@GS shows enhanced kinetics by absorbing 6.01 wt% within just 1.65 min at 290 °C under 15 atm of hydrogen pressure. This is much-improved sorption as compared to MgH_2: FeCoNi and B.M MgH_2 for which hydrogen absorption is 4.41 wt% and 1.45 wt% respectively, under the similar condition of temperature, pressure and time. More importantly, the formation enthalpy of MgH_2: FeCoNi@GS is 58.86 kJ/mol which is 19.26 kJ/mol lower than B.M: MgH_2 (78.12 kJ/mol).

* *Corresponding author.*
E-mail address: heponsphy@gmail.com (O.N. Srivastava).
https://doi.org/10.1016/j.ijhydene.2019.10.204

Excellent cyclic stability has also been found for MgH_2: FeCoNi@GS even up to 24 cycles where it shows only negligible change from 6.26 wt% to 6.24 wt%. A feasible catalytic mechanism of FeCoNi@GS on MgH_2 has been put forward based on X-ray diffraction (XRD), Raman spectroscopy, Fourier Transform Infrared Spectroscopy (FTIR), X-Ray Photoelectron Spectroscopy (XPS), and microstructural (electron microscopic) studies.

Introduction

Increase in environmental degradation level and depletion of fossil fuels results in a crisis of non-renewable energy sources which forced the scientists across the globe to develop new fuel which is renewable, energy-efficient and climate-friendly for production, conversion, and energy storage [1]. It has been observed that among the entire available energy carrier, hydrogen is considered to be one of the clean, environment-friendly and renewable energy vectors. It is well known that during cold combustion in fuel cells and hot combustion in IC engines or turbines, hydrogen energy does not produce carbon dioxide and the dominating combustion product is water which makes hydrogen as the ultimate fuel for avoiding climate change [2,3]. However, the use of hydrogen as a fuel is not straightforward because of its low energy density per unit volume; therefore effective storage of hydrogen is essential. The materials which can be used for hydrogen storage applications must possess, (i) high gravimetric and volumetric density, (ii) manageable thermodynamic properties (30–40 kJ/mol), (iii) fast sorption kinetics, (iv) reversible hydrogen ad/desorption at moderate temperature/pressure (100–120 °C/1–10 atm) conditions, (v) abundance and (vi) low cost, easy and safe to use.

Decades of study [4,5], have shown that storage in the form of hydrides is a viable and effective process. Magnesium hydride (MgH_2) is considered to be a feasible material for mobile as well as stationary applications. MgH_2 has high gravimetric and volumetric hydrogen storage capacity (7.6 wt% hydrogen and 110 g/L hydrogen) [6]. The Abundance of Mg-mineral resources on earth and seawater and its lightweight also makes it a promising material for hydrogen storage applications [7]. But, the high decomposition temperature ($\geq$ 400 °C) and slow de/rehydrogenation kinetics of MgH_2 [8,9] are the issues which need to be improved. Several methods have been used to overcome these drawbacks, such as alloying [10–12], nano-scaling [13–15], mixing with other components [16,17] and use of catalyst [2,18–22]. It has been reported earlier [22,23], that catalyzing MgH_2 by catalysts like metallic species, particularly using transition metals enhance the hydrogen desorption kinetics and decrease the dehydrogenation temperature of MgH_2. Liang et al. [22], reported an enhancement in reaction kinetics of Mg–H system by using transition metals like Ti, V, Mn, Ni and Fe as a catalyst. Hanada et al. [23], have shown that there is an effective decrement in dehydrogenation temperature of MgH_2 during cycling on the addition of nanoparticles of Fe, Co, Ni, and Cu metals. Some recent studies have also shown that the hydrogen storage property of Mg/MgH2 system has been improved by either doping or addition of transition metal composite [24–28].

Moreover, graphene-based materials like graphene oxide, graphene sheets, and its functionalized derivatives can serve as promising catalysts for improving the hydrogen storage properties of MgH_2 [19–21,29–32]. Mechanically milled MgH_2 with 5 wt% graphene has shown a relatively reduced dehydrogenation temperature, improved sorption kinetics, and excellent cyclic stability than that of pure-milled MgH_2 [21]. In another study, mechanically milled MgH_2 with 5 wt% Ni@rGO exhibited a significant decrease in activation energy (E_a) compared to MgH_2 [32].

The presence of few-layer reduced graphene oxide on the MgH_2 surface prevented the agglomeration of hydride during cycling, which enhanced the MgH_2 decomposition and cycling stability [32]. Recently Wang et al. [33], have shown that bimetallic catalyst NiCo on rGO work better than the corresponding singular transition metal catalyst [22,23,29–32], for improving the hydrogen-storage performance of MgH_2. In spite of the above studies a suitable catalyst for taking care of sorption kinetics, thermodynamics and reversibility is still a challenging problem.

Keeping the above-described researches, in the present work we proceeded to use the ternary metallic system for catalyzing MgH_2. The present study is focused on the synthesis and catalytic effect of all the 3d transition metals, Fe, Co, and Ni in alloy form i.e. ternary FeCoNi alloy and its graphene templated version i.e. FeCoNi@GS for improving sorption characteristics of MgH_2. The catalytic effect of FeCoNi@GS has been compared with FeCoNi alloy nanoparticle and it has been found that FeCoNi@GS catalyzed MgH_2 offers much-improved hydrogen sorption properties (including cyclability) as compared to FeCoNi catalyzed MgH_2. A feasible catalytic mechanism of FeCoNi@GS and the synergistic effect of catalyst FeCoNi and the co-catalyst GS for improving the hydrogen storage properties of MgH_2 has been put forward based on FTIR, XPS, XRD and TEM studies. To the best of our knowledge, there are no reports available on the deployment of FeCoNi@GS for catalyzing MgH_2.

Experimental section

Synthesis of GS, FeCoNi and FeCoNi@GS

The starting materials used were pure graphite powder, cobalt(II) nitrate hexahydrate [$Co(NO_3)_2 \cdot 6H_2O$], nickel(II) nitrate hexahydrate [$Ni(NO_3)_2 \cdot 6H_2O$] and iron(III) nitrate

nonahydrate [$Fe(NO_3)_3 \cdot 9H_2O$]. The materials were procured from Sigma Aldrich and ethylenediaminetetraacetic acid [EDTA] was procured from Merck. Here we report the synthesis of graphene oxide (GO) by modified Staudenmaire's method [34]. We had further synthesized graphene sheet (GS) from GO with some modification based on the above-said method in our laboratory [20,35].

Nanoparticles of FeCoNi were synthesized by mixing EDTA (10 mM) into double distilled water (100 ml) in a round bottom flask (RBF). Afterward, reflux of the mixture solution was done for 1 h at 60–80 °C by adding 10 mM of $Ni(NO_3)_2 \cdot 6H_2O$. Further, 12 mM of $Co(NO_3)_2 \cdot 6H_2O$ was added in the same RBF and the reaction was continued for 1 h of reflux at the same temperature. Finally, 15 mM of $Fe(NO_3)_3 \cdot 9H_2O$ was added again for 1 h of reflux at the same temperature. After that, the solution was dried at 80 °C until the precipitate gets formed. After drying, the resulting powder was annealed for 1 h at 400 °C in Argon atmosphere to get the final product i.e. ternary FeCoNi alloy nanoparticles (for brevity termed simply as FeCoNi). The resulting alloy nanoparticles were then collected characterized and tested for its application as a catalyst for hydrogen sorption in MgH_2.

For synthesizing graphene templated ternary FeCoNi alloy nanoparticles (FeCoNi@GS), a minor change in the last step of reflux was made i.e. after addition of 15 mM of $Fe(NO_3)_3 \cdot 9H_2O$, GS dispersion in deionized (DI) water (1.5 mg/ml) (by ultrasonication for 6 h) was added to the reaction mixture. The solution so prepared was refluxed for 1 h at 60–80 °C, keeping the other procedure same as stated above.

Synthesis of FeCoNi and FeCoNi@GS catalyzed MgH_2

MgH_2 powder (purity 98%) was purchased from Alfa Aesar. The MgH_2 powder was ball-milled (B.M) together with 5 wt% FeCoNi@GS catalyst under 5 atm hydrogen pressure in a custom fabricated stainless steel vial of volume 250 cm^3, using a Retsch, PM 400 planetary ball-miller at an operating speed of 250 rpm for a period of 24 h. Ball-milling of MgH_2 was done under a hydrogen atmosphere to prevent MgO formation [36]. The ball to powder ratio was kept as 50:1, where the weight of the sample was around 2.1 g. The synthesis procedure of MgH_2 catalyzed by FeCoNi was kept the same (as stated above) for comparative study. Also, the ball milling of the as-received MgH_2 (uncatalyzed) was done under similar conditions as discussed above for comparing the hydrogen storage properties of catalyzed and uncatalyzed MgH_2. All the samples were handled in an argon-filled glove box (mBRAun MB10) with H_2O and O_2 levels less than1ppm.

Characterization techniques

PANalytical Empyrean X-ray diffractometer with a CuK_α beam ($\lambda = 1.5415$ Å) operated at 40 kV and 40 mA (equipped with 2D area detector (255 × 255 pixel) and a graphite monochromator) has been used for structural characterization of the samples. The samples were loaded in an airtight sample holder covered by a thin layer of parafilm (penchiney plastic packing) to protect the sample from contamination (i.e. from oxygen and moisture) Microstructures of the samples were analyzed through bright field imaging and selected area electron diffraction (SAED) using a FEI TECNAI 20 G^2 transmission electron microscope (TEM) at an accelerating voltage of 200 kV. The surface morphology, elemental composition and elemental mapping of the as-prepared samples were examined by scanning electron microscopy (SEM) {FEI, Quanta 200} equipped with energy dispersive X-ray analysis (EDAX) facility. X-ray photoelectron spectra (XPS) were obtained on an X-ray photoelectron spectrometer (AMICUS, Kratos Analytical) using monochromatized Mg-K_α (1253.6 eV) as X-ray source with an instrument resolution of 0.4 eV and pass energy 150 eV. Raman spectroscopy was used to observe vibrational, rotational, and other low-frequency modes using Horiba LabRAM HR800 with Argon LASER light of wavelength 514 nm. Fourier transform infrared spectroscopy (FTIR) was done by using a PerkinElmer FTIR spectrometer (spectrum 100) in transmission mode covering the wave numbers ranging from 500 to 4000 cm^{-1}.

The temperature-programmed desorption (TPD) at a heating rate of 5 °C/min was done to record the dehydrogenation of the samples. Pressure-composition isotherms (PCI) were recorded using automated four-channel volumetric Sieverts type apparatus supplied by Advanced Materials Corporation (Pittsburgh, USA). Rehydrogenation kinetics was measured in soak mode at 15 atm pressure and 290 °C. Dehydrogenation kinetics was measured under release mode. The dehydrogenation kinetics was performed at 290 °C under 1 atm pressure. Thermal analyses of the samples were conducted using a differential scanning calorimetry (DSC 8000, PerkinElmer). The samples were heated from room temperature to about 500 °C with a heating rate of 5, 10, 15 and 20 °C/min under flowing nitrogen (20 ml min^{-1}).

Results and discussion

Structural and microstructural analyses

Fig. 1(a), (b) shows the XRD patterns for FeCoNi and FeCoNi@GS, respectively. Fig. 1(a) is in good accordance with the reported XRD pattern of FeCoNi alloy [37–39]. The most intense diffraction peaks at $2\theta = 44.03°$ and $2\theta = 51.38°$ correspond to (111) and (200) diffraction peaks of the face-centered cubic (FCC) FeCoNi [33]. The XRD pattern of FeCoNi@GS (Fig. 1(b)) shows similar peak positions as that of FeCoNi. The peaks of GS are not visible because GS is present in very small amount and also peaks of GS are shrouded by the peaks from FeCoNi. We have further computed the crystallite size of FeCoNi and FeCoNi@GS nanoparticles (from Fig. 1(a), (b)) respectively, using modified Scherrer formula [40]. The particle size in FeCoNi and FeCoNi@GS alloy is found to be 41.04 nm and 23.67 nm respectively. The smaller particle size in case of FeCoNi@GS indicates that templation of FeCoNi on graphene sheet helps in refining the grain size. Thus FeCoNi with lower particle size can be formed on GS. Smaller particle size provides a higher surface area for hydrogen diffusion, which could lead to the better catalytic activity of FeCoNi@GS.

A typical TEM micrograph of GS is shown in Fig. 2(a). TEM micrograph revealed a wrinkled texture of GS. Fig. 2(a1) shows the representative selected area electron diffraction (SAED) of GS. The observed hexagonal pattern confirms the graphitic

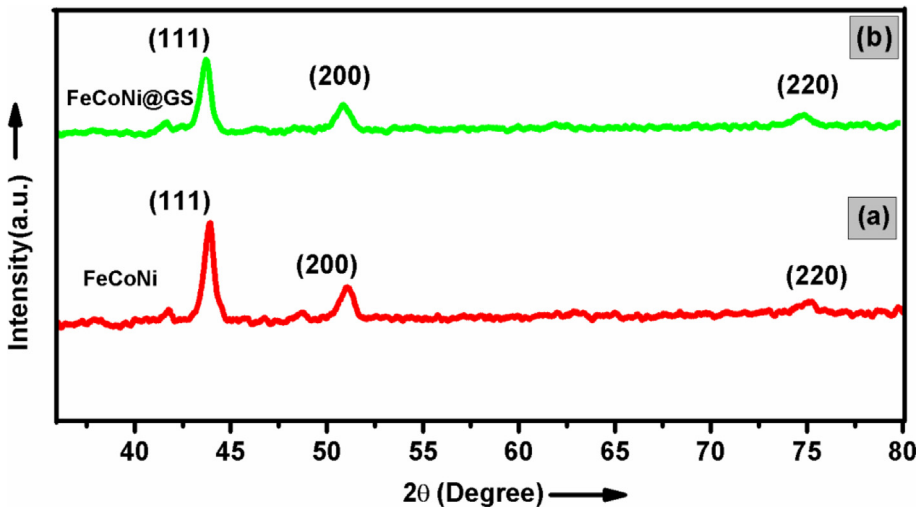

Fig. 1 – XRD pattern of (a) FeCoNi and (b) FeCoNi @GS alloy.

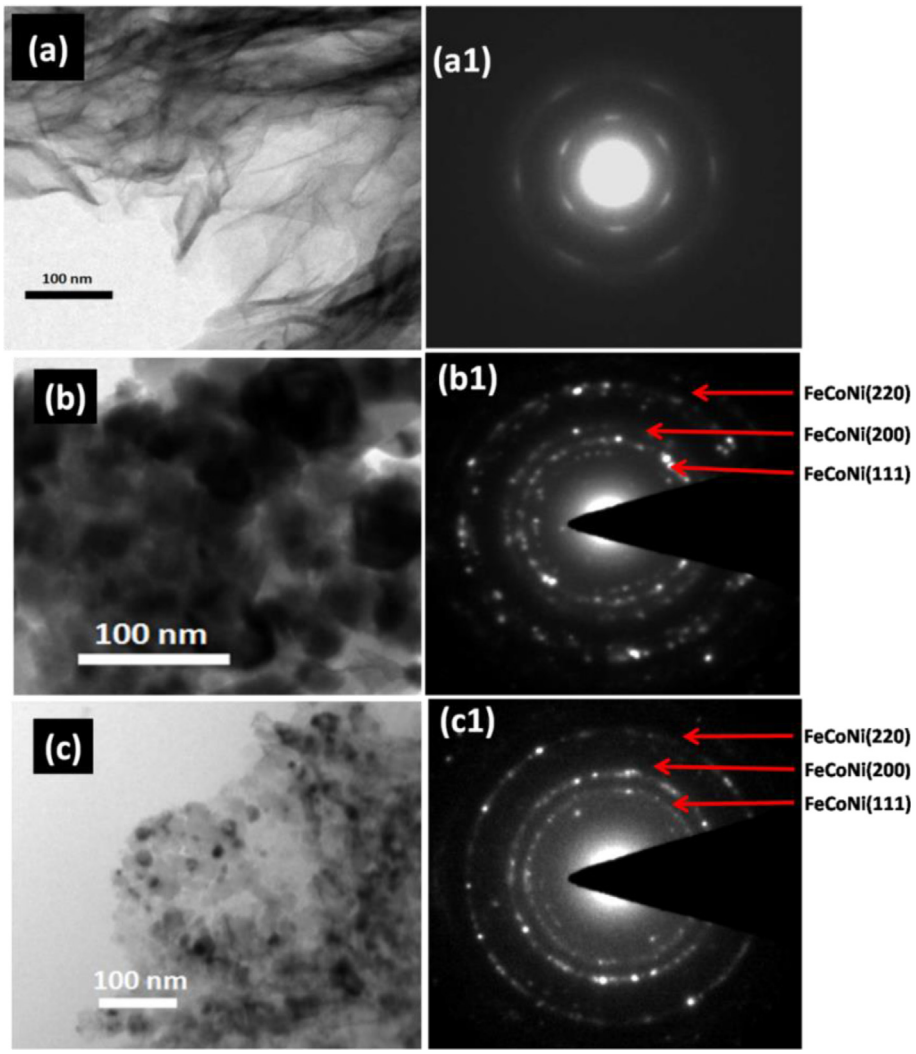

Fig. 2 – TEM micrograph of (a) as synthesized GS (a1) SAED pattern of as synthesized GS (b) TEM micrograph of as synthesized FeCoNi (b1) SAED pattern of as synthesized FeCoNi (c) TEM micrograph of as synthesized FeCoNi@GS (c1) SAED pattern of as synthesized FeCoNi@GS.

nature of the GS. TEM micrograph of FeCoNi (Fig. 2(b)) shows the formation of large clusters of FeCoNi which indicates that FeCoNi nanoparticles are agglomerated. The SAED pattern Fig. 2(b1), clearly shows the rings consisting of distinct spots, indexed as (111), (200), and (220) diffraction peaks from FeCoNi alloy. These matches very well with the diffraction pattern obtained from the powder XRD data (Fig. 1(a)). Fig. 2(c) shows the TEM micrograph of FeCoNi@GS which confirms that FeCoNi particles are nearly uniformly distributed over the surface of GS. The size of FeCoNi nanoparticles is in the range of 5–30 nm. The SAED pattern in Fig. 2(c1) confirms the existence of diffraction rings which can be indexed to the known lattice structure of FeCoNi [41].

Fig. S1 and S2 given in the electronic supplementary information (ESI) section, shows the SEM-EDS elemental mapping of FeCoNi and FeCoNi@GS, respectively. Fig. S1 clearly confirms the presence of all the elements Fe, Co and Ni in FeCoNi alloy. Similarly, Fig. S2 shows the uniform distribution and presence of Fe, Co, Ni together with C in FeCoNi@GS alloy nanoparticles. Figs. S3(a), S3(b) given in ESI section, depict representative FTIR spectra of GS and FeCoNi@GS respectively. In Fig. S3(a) characteristics peaks at 1214 cm^{-1}, 1381 cm^{-1}, 1566 cm^{-1}, and 3088 cm^{-1}can be ascribed to stretching vibration C–O–C, C=C, C–C and O–H stretching mode of intercalated water respectively, which are characteristic peaks of GS [42]. A comparison of Fig. S3(a), Fig. S3(b) reveals the shift of spectral lines (1214 cm^{-1} to 1205 cm^{-1}, 1381 cm^{-1} to 1463 and cm^{-1} and 1566 cm^{-1} to 1693 cm^{-1}). These shifts in spectral lines bring out chemical interaction between FeCoNi and GS.

Fig. 3(a), (b) exhibit typical Raman spectrum of GS and FeCoNi@GS respectively. As is known G band corresponds to in-plane vibration of sp^2 hybridized carbon. The D band represents vibrations of carbon atoms at defect sites including the carbon at the edge atoms forming dangling bonds [43]. A comparison of Fig. 3(a), (b) brings out the fact that for GS I_D/I_G ratio is less than one ($I_D/I_G < 1$) and for FeCoNi@GS I_D/I_G ratio is greater than one ($I_D/I_G > 1$). This reveals the fact that there is a chemical interaction between GS and FeCoNi which leads to displacement of carbon atoms in graphene. This is in keeping with the TEM micrograph shown in Fig. 2(c), where FeCoNi nanoparticles are located on GS pieces.

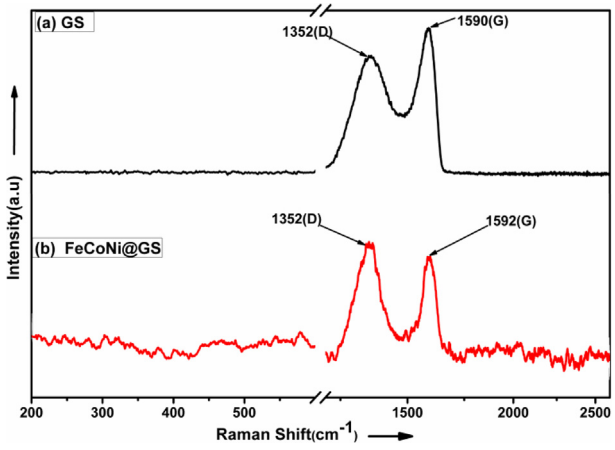

Fig. 3 – Raman spectra of (a) GS and (b) FeCoNi@GS.

Surface chemical and electronic states of FeCoNi and FeCoNi@GS were investigated using X-ray Photoelectron Spectroscopy (XPS) technique. To gain more insight about the electronic states and chemical interactions present at the surface, detailed scan spectrum was recorded corresponding to each element and further deconvoluted using XPSPEAK4.1 software [44]. The binding energy of the observed elements has been tabulated in Table 1.

Fig. 4((a) and (b)) show the deconvoluted spectrum of Fe2p signal for FeCoNi and FeCoNi@GS, respectively. Fe2p spectrum from FeCoNi (Fig. 4(a)) shows satellite signal at 717.6eV arising due to combination of Fe^{2+} and Fe^{3+}, the other spectral peak can be assigned to Fe^{3+}, Fe^{2+} $2p_{3/2}$ (709.5eV), Fe^{3+} $2p_{3/2}$ (712.5eV) and Fe^{2+} $2p_{1/2}$ (722.6eV) whereas the spectra for FeCoNi@GS (Fig. 4(b)) show the presence of $Fe^{2+}2p_{3/2}$ (709.8eV), instrumental artifact (704.0eV), Fe^{2+} $2p_{1/2}$ (722.9eV) and Fe^{3+} $2p_{1/2}$, satellite peak (728.5eV) signals [33,45]. The above discussion clearly indicates the change in the electronic states of Fe2p in FeCoNi@GS as compared to that of FeCoNi.

Fig. 4 ((c) and (d)) show the deconvoluted spectrum of Co2p signal for FeCoNi and FeCoNi@GS, respectively. The deconvoluted Co2p spectrum for FeCoNi (Fig. 4(c)) depicts Co^0 (778.7eV), Co^{2+} $2p_{3/2}$ (781.2eV), satellite peak due to Co (785.0eV) along with a shoulder peak $Co2p_{3/2}$ (788.3eV). The other B.E. positions at 796.0eV and 797.7eV correspond to $Co^{3+}2p_{1/2}$ and $Co^{2+}2p_{1/2}$, respectively. The deconvoluted spectrum of FeCoNi@GS shows a slight shift in the B.E positions to 779.5eV (Co^0), 783.2eV ($Co^{2+}2p_{3/2}$), 795.4eV ($Co^{2+}2p_{1/2}$), 797.8eV ($Co^{3+}2p_{1/2}$) along with a satellite peak ~ 787.0eV [46–48]. Here again the changes in the electronic state of Co2p in FeCoNi@GS as compared to that of FeCoNi can be easily observed.

Fig. 4((e) and (f)) show the deconvoluted spectrum of Ni2p signal for FeCoNi and FeCoNi@GS, respectively. The spectra of FeCoNi (Fig. 4(e)) shows the B.E. positions at ~852.6eV (metallic Ni), 855.4eV ($Ni^{2+}2p_{3/2}$), 872.4eV ($Ni^{2+}2p_{1/2}$), 875.0eV ($Ni2p_{1/2}$, satellite), along with the presence of satellites peaks at 861.1eV and 866.8eV. Moreover, the spectra for FeCoNi@GS shows a shift in the B.E. positions as compared to FeCoNi with peak positions at 849.2eV (Ni Auger signal), 854.5eV ($Ni^{2+}2p_{3/2}$), 858.2eV (satellite signal due to NiO) and 869.9eV ($Ni^{2+}2p_{1/2}$). The spectrum also shows a satellite peak at 862.1eV along with auger signal at 867.8eV [48–50]. Similar to above XPS spectra of Fe2p and Co2p the changes in the electronic state of Ni2p in FeCoNi@GS is evident when FeCoNi is templated on GS.

Deconvoluted spectra of C1s

The deconvoluted spectrum of C1s (Fig. 4(g)) corresponds to C (π-π) (291.6eV), C=O (289.85eV), C-OR (285.68eV) [51], indicates different chemical state of C derived from FeCoNi@GS.

The above observed results in the case of Fe2p, Co2p and Ni2p (Fig. 4) indicate the changes in the electronic states of FeCoNi@GS as compared to FeCoNi due to shift in B.E positions and existence of altogether new peaks (e.g. 704.0eV, 728.5eV, 779.50eV, 783.20eV, 787.0eV, 797.8eV, 858eV, 866.8eV and 867.8eV) in FeCoNi@GS sample in comparison to (709.5eV, 722eV, 778.70eV, 781.20eV, 785.0eV, 796.0eV, 855eV, 861.0eV and 862.10eV) peaks of FeCoNi samples listed in Table 1. This clearly shows the electronic interaction between GS and

Table 1 – Binding energies of Fe2p, Co2p, Ni2p in FeCoNi and FeCoNi@GS.

Identified Peak positions		
States	a. FeCoNi	b. FeCoNi@GS
Fe2p	i. 717.6eV (satellite peak due to $2p_{3/2}$)	i. 709.8eV (Fe^{2+} $2p_{3/2}$)
	ii. 709.5eV (Fe^{2+} $2p_{3/2}$)	ii. 704.0eV (Instrumental Artifact)
	iii. 712.5eV (Fe^{3+} $2p_{3/2}$)	iii. 722.9eV (Fe^{2+} $2p_{1/2}$)
	iv. 722.6eV (Fe^{2+} $2p_{1/2}$)	iv. 728.5eV (Fe^{3+} $2p_{1/2}$, satellite peak)
Co2p	i. 778.7eV (Metallic Co^0)	i. 779.5eV (metallic Co^0)
	ii. 781.2eV (Co^{2+} $2p_{3/2}$)	ii. 783.2eV ($Co^{2+}2p_{3/2}$)
	iii. 785.0eV (satellite peak due to Co)	iii. 795.4eV ($Co^{2+}2p_{1/2}$)
	iv. 788.3eV ($Co2p_{3/2}$)	iv. 797.8eV ($Co^{3+}2p_{1/2}$)
	v. 796.0eV ($Co^{3+}2p_{1/2}$)	v. 787.0eV (satellite peak)
Ni2p	i. 852.6eV (metallic Ni)	i. 849.2eV (Ni Auger signal)
	ii. 855.4eV ($Ni^{2+}2p_{3/2}$)	ii. 854.5eV ($Ni^{2+}2p_{3/2}$)
	iii. 872.4eV ($Ni^{2+}2p_{1/2}$)	iii. 858.2eV (satellite signal due to NiO)
	iv. 875.0eV ($Ni2p_{1/2}$satellite)	iv. 869.9eV ($Ni^{2+}2p_{1/2}$)
	v. 861.1eV (satellite peak)	v. 862.1eV (satellite peak)
	vi. 866.8eV (satellite peak)	vi. 867.8eV (auger signal)

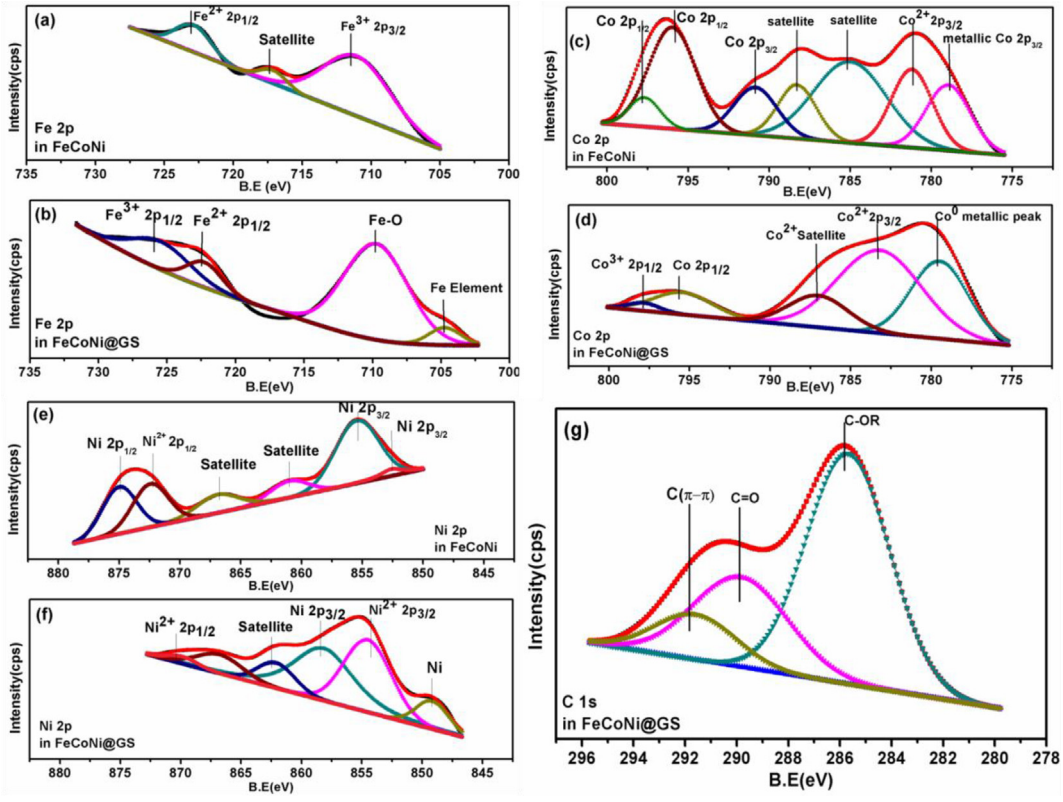

Fig. 4 – XPS spectra of (a–b) Fe2p from FeCoNi alloy and FeCoNi@GS (c–d) Co2p from FeCoNi and FeCoNi@GS alloy (e–f) Ni2p from FeCoNi and FeCoNi@GS alloy and (g) C1s from FeCoNi@GS.

FeCoNi alloy. This interaction will further ease the electron transfer between FeCoNi@GS and MgH_2.

Hydrogen sorption analysis of catalyzed MgH_2-study of kinetics

Comparative TPD profiles of B.M MgH_2 (un-catalyzed), MgH_2+5 wt% FeCoNi and MgH_2+5 wt% FeCoNi@GS (catalyzed) are shown in Fig. 5(i). B.M MgH_2 has an onset desorption temperature of 355 °C and full desorption (6.60 wt%) gets completed at ~ 420 °C. While the TPD profile of MgH_2+5 wt% FeCoNi has onset dehydrogenation temperature of ~280 °C and at ~380 °C full dehydrogenation gets completed. In contrast, the onset dehydrogenation temperature of MgH_2+5 wt% FeCoNi@GS is ~255 °C and it releases 6.10 wt% hydrogen up to 350 °C. From the above discussions, it is clear

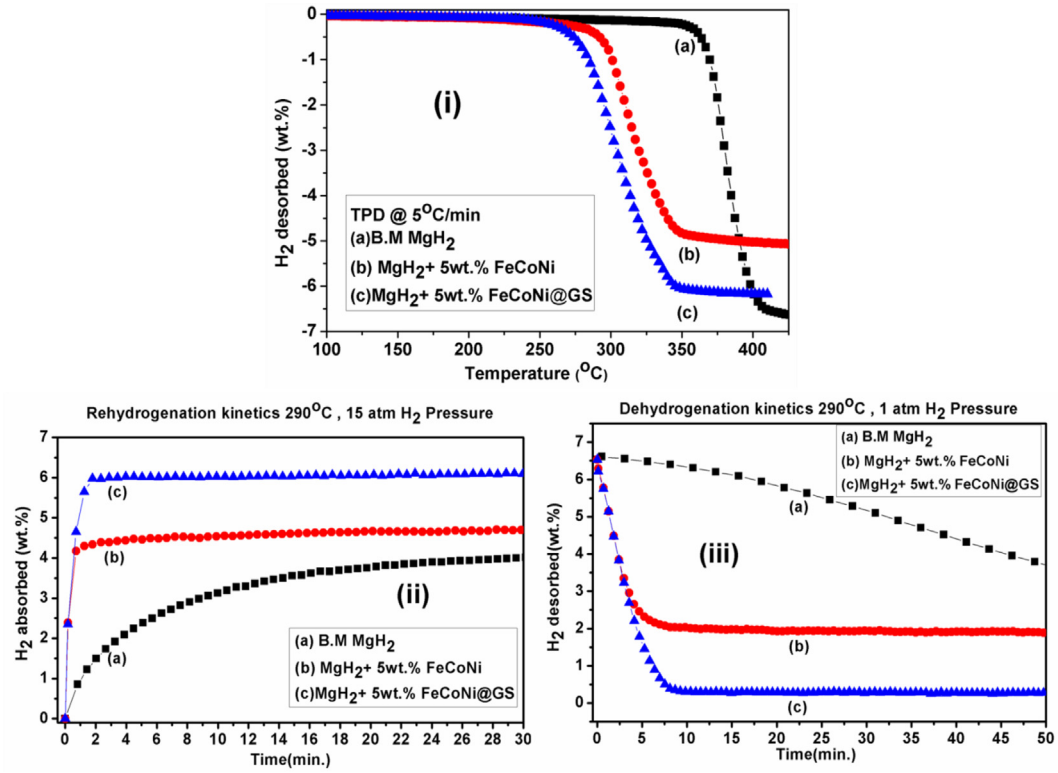

Fig. 5 – (i) TPD profile of (a) B.M MgH_2 (b) MgH_2+5 wt%FeCoNi (c) MgH_2+5 wt%FeCoNi @GS (ii) Rehydrogenation Kinetics curve of (a) B.M MgH_2 (b) MgH_2+5 wt%FeCoNi (c) MgH_2+5 wt%FeCoNi @GS at 290 °C at 15 atm (iii) Dehydrogenation Kinetics curve of (a) B.M MgH_2 (b) MgH_2+5 wt%FeCoNi (c) MgH_2+5 wt%FeCoNi @GS at 290 °C at 1 atm.

that the initial dehydrogenation temperature for MgH_2+5 wt% FeCoNi@GS is 100 °C and 25 °C lower than B.M MgH_2 and FeCoNi catalyzed MgH_2, respectively.

In order to examine the reversibility of catalyzed MgH_2, the rehydrogenation (Fig. 5(ii)) was carried out at 290 °C under 15 atm hydrogen pressures. From Fig. 5(ii), it can be observed that the B.M MgH_2 absorbs 1.45 wt% hydrogen within 1.65 min, whereas FeCoNi catalyzed MgH_2 is found to absorb 4.40 wt% of hydrogen under the similar condition of temperature and pressure within 1.65 min. Moreover, as compared to B.M MgH_2 and FeCoNi catalyzed MgH_2, MgH_2 catalyzed by FeCoNi@GS shows better reversibility, as it absorbs 6.01 wt% hydrogen within 1.65 min. Thus, it can be concluded that MgH_2+5 wt% FeCoNi@GS absorbs 1.6 wt% more hydrogen as compared to FeCoNi catalyzed MgH_2 under identical conditions of pressure and temperature.

For checking the dehydrogenation kinetics of MgH_2, the rehydrogenated MgH_2 (B.M and catalyzed both) was dehydrogenated at 290 °C under 1 atm pressure of hydrogen. It is clearly observed from Fig. 5(iii), that B.M MgH_2 released 0.25 wt % hydrogen within 8.5 min while FeCoNi catalyzed MgH_2 desorbs 4.47 wt% in 8.5 min at 290 °C under 1 atm pressure of hydrogen. While MgH_2+5 wt% FeCoNi@GS desorbs 6.14 wt% hydrogen within 8.5 min under similar conditions. The observed results show the improved catalytic effect of FeCoNi@GS over FeCoNi for de/rehydrogenation studies. Thus, from the study, it can be concluded that FeCoNi@GS shows an excellent catalytic effect on MgH_2 for both hydrogen desorption and absorption.

For understanding the improvement in dehydrogenation kinetics of the rehydrogenated MgH_2, the activation energy barrier in the presence of catalysts FeCoNi and FeCoNi@GS were determined by evaluating the data obtained from DSC. It is to be noted that the DSC was performed in the presence of flowing nitrogen (20 ml min^{-1}) at heating rates (5 °C min^{-1}, 10 °C min^{-1}, 15 °C $min^{-1}$and 20 °C min^{-1}) while TPD was done under vacuum @5 °C min^{-1}. There is a difference of onset hydrogen desorption temperature in DSC (Fig. S4(i) in ESI section and Fig. 6(i)) and TPD (Fig. 5(i) (b and c)) curves, for MgH_2: FeCoNi and MgH_2: FeCoNi @GS respectively.

The samples were heated at different heating rates (5, 10, 15 and 20 °C/min) to obtain the activation energy using DSC curves. To find activation energy by using Kissinger equation [52], given below, the peak desorption temperature at the corresponding heating rate was then used.

$$\ln\left(\beta / T_P^2\right) = \left(-E_a / RT_P\right) + \ln\left(K_o\right) \quad (1)$$

where T_p is the corresponding peak desorption temperature and β is the heating rate. The slope obtained from the plot between ln (β/T_p^2) and $1000/T_p$ (shown in Fig. S4(ii) in ESI section and Fig. 6(ii)) is used for calculating the desorption activation energy. The activation energy thus obtained for MgH_2: FeCoNi was found to be 90.24 kJ/mol (Fig. S4) while activation energy for MgH_2: FeCoNi@GS was 85.14 kJ/mol. This signifies the better catalytic action of FeCoNi@GS over FeCoNi nanoparticles. The activation energy barrier is lowered by 5.1 kJ/mol in case of MgH_2 catalyzed by FeCoNi@GS. The activation energy of 85.14 kJ/mol simply implies that we have to give

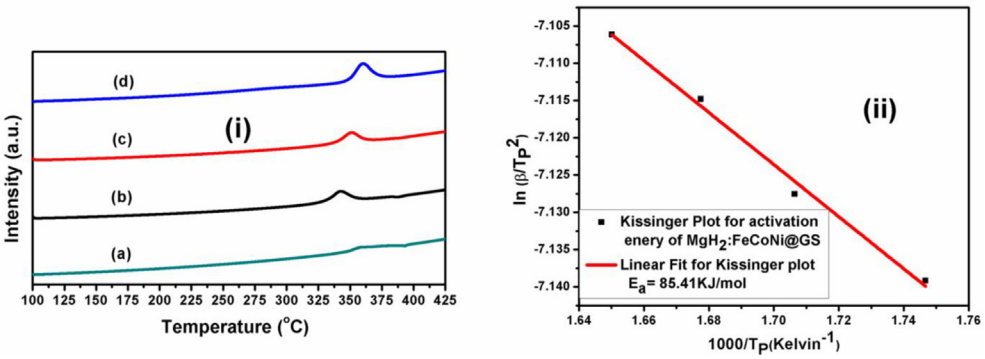

Fig. 6 – (i) DSC profile of MgH_2 catalyzed by FeCoNi@GS heated at (a) 5 °C min^{-1} (b) 10 °C min^{-1} (c) 15 °C min^{-1}, and (c) 20 °C min^{-1} (ii) Kissinger plot for evaluating activation energy.

85.14 kJ/mol energy to overcome the energy barrier for the conversion of MgH_2 into Mg in case of MgH_2 catalyzed by FeCoNi@GS. The activation energy found in the present study is significantly lower than that for bimetallic NiCo catalyzed MgH_2 (105 kJ/mol) [33].

Hydrogen sorption analysis of catalyzed MgH_2-study of thermodynamics

Based on the discussions from the previous sections, it can be easily concluded that FeCoNi@GS has better catalytic action as compared to FeCoNi. It will, therefore, be taken as an optimum catalyst. We proceeded further to check the effect of FeCoNi@GS on the thermodynamics of conversion of MgH_2 to Mg. Fig. 7(i) shows the PCI isotherms and Fig. 7(ii) and (iii) represent the Van't Hoff plots for absorption and desorption, respectively of MgH_2: FeCoNi@GS. The absorption plateau pressures were found to be 2.03 atm, 3.88 atm, 4.54 atm and 5.80 atm at 270 °C, 285 °C, 300 °C, and 315 °C temperatures, respectively whereas, the desorption plateau pressures were found to be 0.41 atm, 2.36 atm, 3.17 and 5.03 atm at 270 °C, 285 °C, 300 °C, and 315 °C respectively. From Fig. 7(ii) and (iii), the slope and intercept of the Van't Hoff plot gives the enthalpy and entropy values, respectively of MgH_2: FeCoNi@GS.

For the formation of MgH_2 (absorption) the changes in enthalpy and entropy values for MgH_2: FeCoNi@GS are found to be 58.86 kJ per mol of H_2 and 115.31 J k^{-1} per mol of H_2,

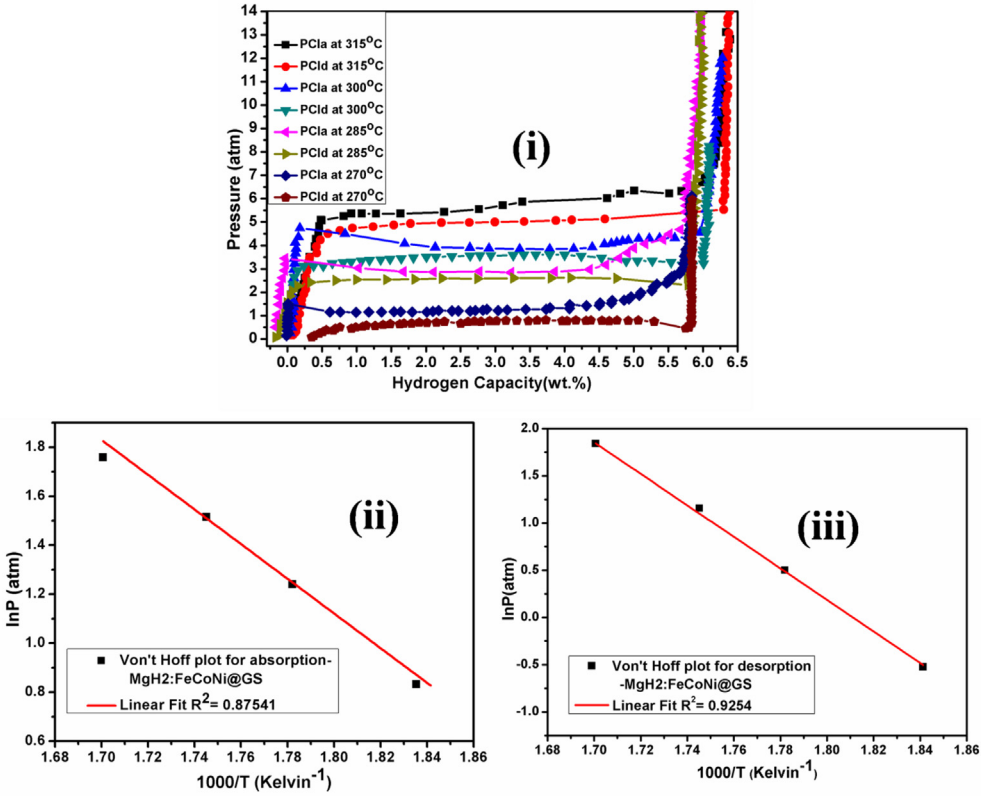

Fig. 7 – (i) PCI absorption and desorption curves of MgH_2: FeCoNi@GS determined at different temperatures, (ii) Van't Hoff plot for absorption of MgH_2: FeCoNi@GS, and (iii) Van't Hoff plot for desorption of MgH_2: FeCoNi@GS.

respectively. The change in desorption enthalpy and entropy values are found to be 61.02 kJ per mol of H_2 and 121.69 J k^{-1} per mol of H_2, respectively. It was found that the change in formation enthalpy and entropy values for the B.M MgH_2 is 78.12 kJ per mol of H_2 and 133.40 JK^{-1}per mol of H_2, respectively. This implies that the thermodynamics barrier for MgH_2: FeCoNi@GS (for absorption) gets lowered by 19.26 kJ/mol of H_2 (for enthalpy) and 18.09 $Jk^{-1}mol^{-1}$ of H_2 (for entropy) as compared to B.M MgH_2. The change in formation enthalpy of 19.26 kJ/mol of H_2 as compared to B.M MgH_2 can be attributed to modified interfacial effect which is created on ball milling of MgH_2 with FeCoNi@GS. It is well known that the change in interface energy of MgH_2 with catalyst will affect the enthalpy values [4,53].

Hydrogen sorption analysis of catalyzed MgH_2-cycling study

In hydrogen sorption analysis of catalyzed MgH_2-study of kinetics and hydrogen sorption analysis of catalyzed MgH_2-study of thermodynamics, we have shown that FeCoNi@GS has a substantial effect on the kinetics and thermodynamics of hydrogen sorption in MgH_2. Therefore, we proceeded to check the cyclic stability of MgH_2: FeCoNi@GS. For checking the cyclic stability of MgH_2 catalyzed by FeCoNi@GS, continuous rehydrogenation and dehydrogenation at the temperature and pressure discussed above were performed. Fig. 8 shows the hydrogen storage capacity of MgH_2: FeCoNi@GS up to 24 cycles of de/rehydrogenation.

Interestingly even after 24 cycles of de/rehydrogenation, there is hardly any change in the hydrogen storage capacity of MgH_2: FeCoNi@GS (from 6.26 wt% to 6.24 wt%). Thus, it can be said that MgH_2: FeCoNi@GS shows excellent cyclic stability. The feasible reason for this improved kinetics, thermodynamics and cyclic stability of Mg/MgH_2 is discussed in the following section.

Catalytic mechanism of FeCoNi@GS on MgH_2

MgH_2 exhibits an ionic-covalent bond with more ionic character than covalent [54] and having charge densities as $Mg^{1.509+}$ and $H^{0.754-}$, since Mg is partially ionized; the remaining charge of Mg contributes to the covalent bonding in

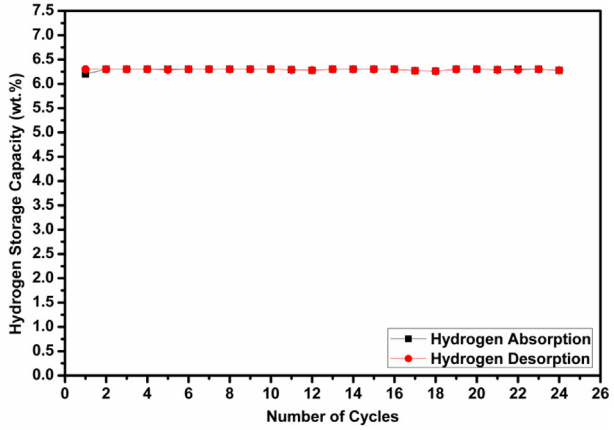

Fig. 8 – Cyclic (de/rehydrogenation) characteristic curve of MgH_2: FeCoNi@GS at 290 °C.

MgH_2 [55]. The ionic-covalent bonding in MgH_2which itself explains the high stability of this material [55]. In order to address the problem of high stability and thus high de/re-hydrogenation enthalpy, it has been well known that nanostructuring and addition of catalyst/dopant are general methods [56]. Theoretical calculations predicted that nanostructuring, via ball milling, will improve thermodynamic properties if one can synthesize MgH_2 as molecular size units, and larger units are less stable than the bulk [57–60]. Shevlin et al. [60] studied the structural and thermodynamic properties of a variety of $(MgH_2)_n$ clusters, where n = 1–100 and demonstrated that nanostructuring at these sizes did not improve dehydrogenation thermodynamics.

It is clear from recent theoretical and experimental finding [57–60] that the nanostructuring will not make MgH_2 candid for practical applications and the catch lies in the design of catalyst and understanding its catalytic properties. This will eventually help in the further development of new catalyst and improving the de/re-hydrogenation properties of MgH_2, so as to make it compatible for on-board hydrogen storage application. Theoretical calculations by Khatabi et al. [61] shows that the bonding between Mg and H can be weakened by using suitable catalyst/additive (particularly 3d and 4d transition metals). They show the decrement in the charge density on Mg and H by the introduction of 3d and 4d transition metals with MgH_2. This decrement of the charge density induces a decrease of the charge transfer between Mg and H, which consequently leads to the destabilization of MgH_2. It is also noteworthy to point out that the decrease of Mg and H charge densities follows the same decreasing order of the heat of formation and desorption temperature for MgH_2. Larrson et al. [62] calculated the charge deformation density in order to understand the effects of Ni dopants on the electronic structure of the MgH_2 clusters and thus the mechanism behind the reduced removal energy in case of Ni (or Fe) doped MgH_2. According to Larrson et al. [62] the reduction of the H– anion charge in Mg–H by the introduction of Ni (or Fe) will weaken the bonding between Mg and H which further decreases the stability of Mg–H bond and enthalpy of dehydrogenation.

It has also been observed that there exists robust hybridization between H and Mg atoms near the Fermi level, which indicates the sturdy interaction between H and Mg atoms. On the other hand, for transition metal-doped system there are few energy bands across d orbital of the dopant and the s orbital's of hydrogen are reduced at the Fermi level, thus the hybridization between H and Mg atoms is weaker compared to the pure system [63]. Furthermore, it was noted that the activity of transition metal alloy can be notably enhanced when doping third metal in the binary structure. Enhancement in the catalytic activity of the FeCoNi catalyst (as compared to stand-alone Fe, Co, Ni or binary system) has been found which can be attributed to the partial-charge transfer activation effect induced by Fe species to activate Ni or Co in the ternary system [64]. Incorporation of third metal in the binary alloy promotes the multi-electron transportation process which leads to change of oxidation state of metal from lower to higher value. Keeping above mentioned theoretical studies in view and based on our experimental (structural, microstructural and XPS characterization) findings, we proceed to propose the most feasible catalytic action based on the results in

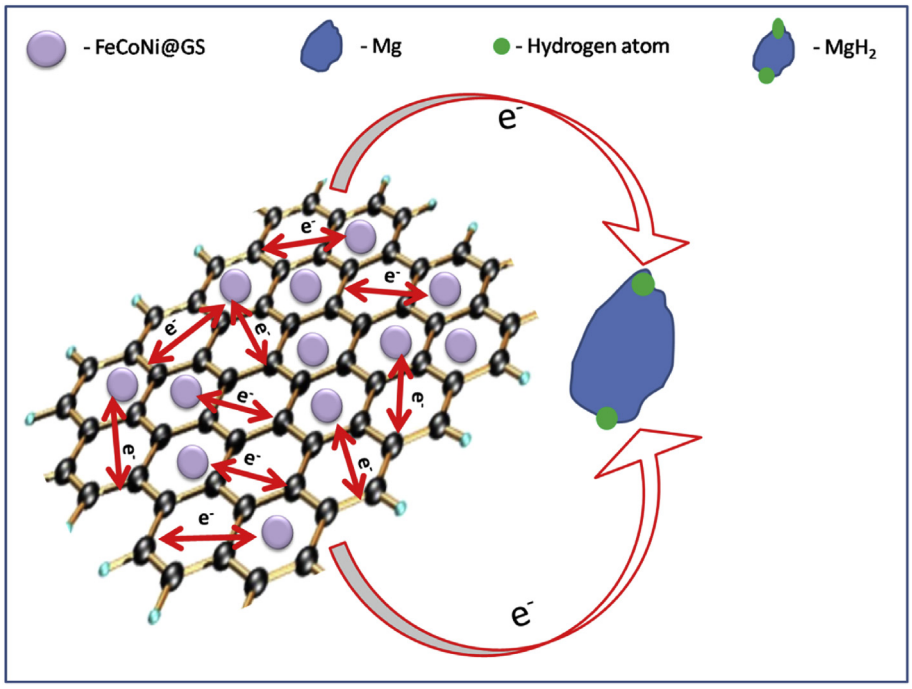

Fig. 9 – Schematic illustration of catalytic mechanism of FeCoNi@GS.

the foregoing section clearly show that FeCoNi@GS works as an excellent catalyst for hydrogen sorption in MgH_2.

The presence of three different 3d type transition metals produces synergistic effect amongst them, which leads to electron transfer, to and fro from FeCoNi to MgH_2. Also, the 3d type alloys templated on graphene exhibit better catalytic effect because of electronic interaction between graphene and FeCoNi nanoparticles which leads to feasible transfer of electrons between ternary alloy and graphene sheet. This fact has been confirmed through XPS (Fig. 4) where it has been shown that the electronic state of Fe, Co and Ni changes upon interaction with graphene. This indicates the electronic interaction between GS and FeCONi.

Based on known results, it can be said that the interaction between FeCoNi and GS results in synergetic effect making MgH_2 sorption more conducive. Notably, the electronic interaction between FeCoNi@GS and MgH_2 will make the electronic interaction between FeCoNi and GS also between FeCoNi@GS and MgH_2 will decrease the electronic charge density between Mg and H. This will eventually affect the Mg–H bond strength and thus lowers the dehydrogenation enthalpy. The electronic interaction between FeCoNi and GS also between FeCoNi@GS and MgH_2 is shown schematically in Fig. 9.

Another effect which has not been explicitly outlined, regarding graphene templation is in regard to its influence on agglomeration. TEM micrographs (Fig. 2(b) and (c)), are suggestive of the fact that graphene templation leads to the anchoring of FeCoNi catalyst on the graphene sheet. It checks agglomeration of catalyst nanoparticles. This leads to sustainability of FeCoNi nanoparticles during cycling and is in keeping with very good cyclability obtained for de/rehydrogenation of MgH_2: FeCoNi@GS.

Fig. 10 shows the structural characterization of the MgH_2: FeCoNi@GS before and after 24 cycles of de/rehydrogenation. Fig. 10(a) shows the XRD pattern of as-milled MgH_2: FeCoNi@GS which mainly shows the presence of MgH_2 diffraction peaks together with FeCoNi. This implies that MgH_2 was well-maintained during the milling. Fig. 10(b) shows the XRD pattern of dehydrogenated MgH_2: FeCoNi@GS after 24 cycles. The XRD patterns of dehydrogenated MgH_2: FeCoNi@GS shows the presence of both Mg and FeCoNi. This shows the complete dehydrogenation of MgH_2. The complete transformation between MgH_2 and Mg explains the well-maintained hydrogen storage capacity during cycling. Moreover, the peaks at 44.03° and 51.38° correspond to the (111) and (200) diffraction peaks of the FeCoNi phase, thus indicating that FeCoNi@GS survives during the cycling. To further look

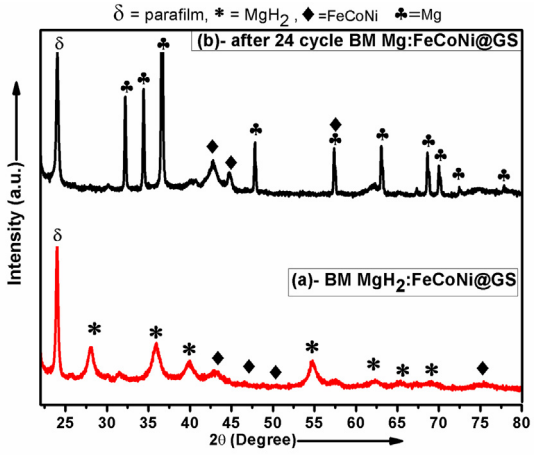

Fig. 10 – XRD curve of (a) MgH_2: FeCoNi@GS after ball milling, (b) Mg: FeCoNi@GS after 24 cycle.

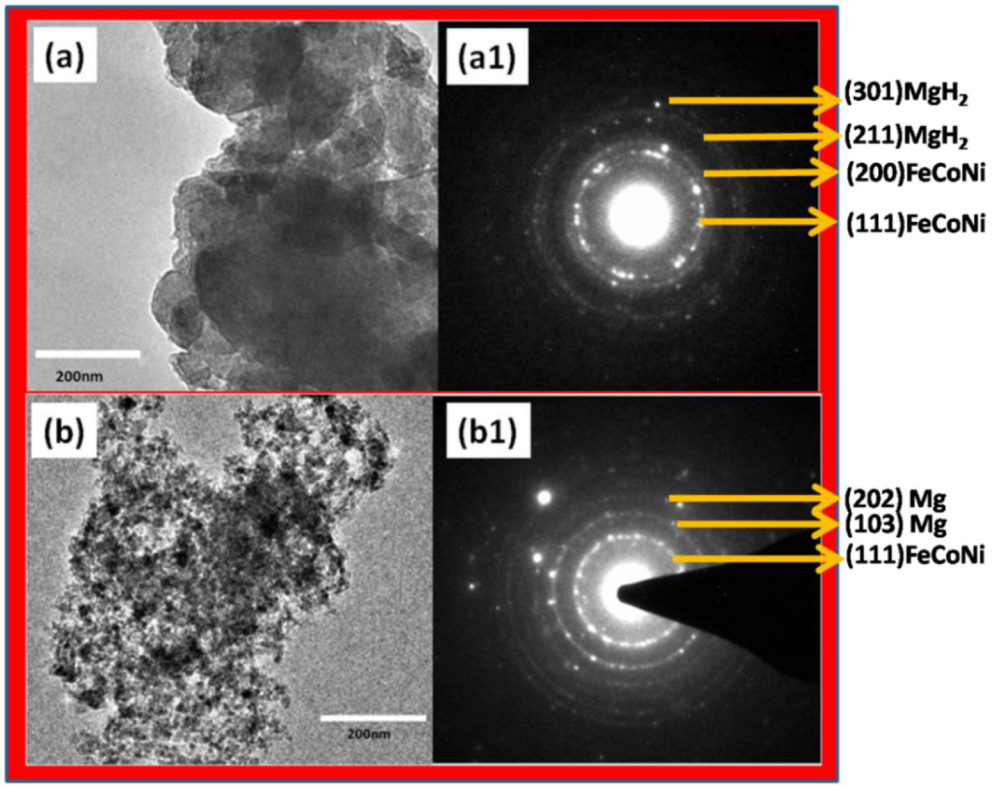

Fig. 11 – TEM micrograph of (a) MgH_2: FeCoNi@GS, (a1) SAED pattern of MgH_2: FeCoNi@GS, (b) TEM micrograph of Mg: FeCoNi@GS after 24 cycles, (b1) SAED pattern of Mg: FeCoNi@GS after 24 cycles.

into the microstructure of MgH_2: FeCoNi@GS a TEM study was performed.

Fig. 11 shows a representative TEM micrograph and the related SAED pattern of MgH_2: FeCoNi@GS (dehydrogenated) after 24 cycles. It is clear that the FeCoNi@GS even after 24 cycles (Fig. 11(b)) is homogeneously dispersed and no agglomeration of Mg/MgH_2 particles could be seen. Furthermore, Fig. 11(a1) and (b1) represents SAED patterns of the catalyzed MgH_2: FeCoNi@GS and Mg: FeCoNi@GS (after 24 cycles) which shows MgH_2 and Mg respectively together with FeCoNi, similar to what we have observed in XRD studies (Fig. 10). Thus based on the above discussions, it can be concluded that the templation of GS over FeCoNi leads to modified electronic interaction, nearly uniform distribution of FeCoNi over GS and lack of agglomeration of FeCoNi during cycling. All these factors provide better catalytic properties to FeCONi@GS.

Conclusions

The catalytic action of the graphene sheet (GS) templated FeCoNi alloy nanoparticles (FeCoNi@GS) has been utilized for improving the hydrogen sorption in MgH_2. It has been found that FeCoNi@GS has superior catalyst activity as compared to FeCoNi alloy. The FeCoNi@GS catalyzed MgH_2 has an onset desorption temperature of ~255 °C while MgH_2: FeCoNi have onset desorption temperature of ~280 °C. The superior catalytic properties of FeCoNi@GS also persist in the rehydrogenation study. Additionally, the kinetic and thermodynamic barrier for MgH_2: FeCoNi@GS were found to be 85.14 kJ/mol (activation energy) and 58.86 kJ/mol of H_2 (formation enthalpy) respectively. These are considerably lower as compared to pristine MgH_2. Structural (X-ray diffraction (XRD)), microstructural, and Raman spectroscopic studies show that GS as a template ensures the uniform distribution of catalyst FeCoNi. Also, templation avoids their agglomeration and increases the durability, electronic interactions, and stability of the catalyst. Thus, the catalyst remains stable even after 24 cycles of de/rehydrogenation. The present study suggests that the ternary alloys of transition metals templated on graphene improve catalytic effect for hydrogen sorption in MgH_2. This improvement corresponds to the better catalytic performance in comparison to the corresponding graphene templated bimetallic alloy as well as the non-templated ternary alloy. The results obtained in the present investigation suggests that the alloy which is feasible to be synthesized from more than two transition metals (ternary, quaternary and still higher metal component alloys) template on graphene may emerge as a new class of catalyst for the most potential hydrogen storage material MgH_2. Such alloys may favorably change the kinetics, thermodynamics, and cyclability of MgH_2 and make it a viable hydrogen storage system for applications.

Acknowledgements

Financial support from the Ministry of New and Renewable Energy (Mission mode project on Hydrogen Storage), DST (FIST), DRDO and the University Grants Commission are

thankfully acknowledged. The author would also like to acknowledge Prof. Pankaj Srivastava (Department of Chemistry, Banaras Hindu University) for helpful discussions.

Appendix A. Supplementary data

Supplementary data to this article can be found online at https://doi.org/10.1016/j.ijhydene.2019.10.204.

REFERENCES

[1] Liu W, Setijadi E, Crema L, Bartali R, Laidani N, Aguey-Zinsou KF, Speranza G. Carbon nanostructures/Mg hybrid materials for hydrogen storage. Diam Relat Mater 2018;82:19–24.

[2] Bhatnagar A, Pandey SK, Vishwakarma AK, Singh S, Shukla V, Soni PK, Shaz MA, Srivastava ON. Fe3O4@Graphene as a superior catalyst for hydrogen de/absorption from/in MgH2/Mg. J Mater Chem A 2016;4:14761–72.

[3] Tozzini V, PelleGsini V. Prospects for hydrogen storage in graphene. Phys Chem Chem Phys 2013;15:80–9.

[4] Bhatnagar A, Johnson JK, Shaz MA, Srivastava ON. TiH_2 as a dynamic additive for improving the de/rehydrogenation properties of MgH_2: a combined experimental and theoretical mechanistic investigation. J Phys Chem C 2018;122:21248–61.

[5] Pandey SK, Bhatnagar A, Mishra SS, Yadav TP, Shaz MA, Srivastava ON. Curious catalytic characteristics of Al–Cu–Fe quasicrystal for de/rehydrogenation of MgH_2. J Phys Chem C 2017;121:24936–44.

[6] Zhang L, Xiao X, Xu C, Zheng J, Fan X, Shao J, Li S, Ge H, Wang Q, Chen L. Remarkably improved hydrogen storage performance of MgH_2 catalyzed by multivalence NbH_x nanoparticles. J Phys Chem C 2015;119:8554–62.

[7] Ma Z, Zhang J, Zhu Y, Lin H, Liu Y, Zhang Y, Zhu D, Li L. Facile synthesis of carbon supported nano-Ni particles with superior catalytic effect on hydrogen storage kinetics of MgH_2. ACS Appl Energy Mater 2018;3:1158–65.

[8] Bhatnagar A, Pandey SK, Dixit V, Shukla V, Shahi RR, Shaz MA, Srivastava ON. Catalytic effect of carbon nanostructures on the hydrogen storage properties of MgH_2–$NaAlH_4$ composite. Int J Hydrogen Energy 2014;39:14240–6.

[9] Wang Y, Li L, An C, Wang Y, Chen C, Jiao L, Yuan H. Facile synthesis of TiN decorated graphene and its enhanced catalytic effects on dehydrogenation performance of magnesium hydride. Nanoscale 2014;6:6684.

[10] Liu H, Wang X, Liu Y, Dong Z, Cao G, Li S, Yn M. Improved hydrogen storage properties of MgH_2 by ball milling with AlH_3: preparations, de/rehydriding properties, and reaction mechanisms. J Mater Chem 2013;1:12527.

[11] Mahmoudi N, Kaflou A, Simchi A. Hydrogen desorption properties of MgH_2–$TiCr_{1.2}Fe_{0.6}$ nanocomposite prepared by high-energy mechanical alloying. J Power Sources 2011;196:4604–8.

[12] Si T, Cao Y, Zhang Q, Sun D, Ouyang L, Zhu M. Enhanced hydrogen storage properties of a Mg–Ag alloy with solid dissolution of indium: a comparative study. J Mater Chem 2015;3:8581–9.

[13] Jeon KJ, Moon HR, Ruminski AM, Jiang B, Kisielowski C, Bardhan R, Urban JJ. Air-stable magnesium nanocomposites provide rapid and high-capacity hydrogen storage without using heavy-metal catalysts. Nat Mater 2011;10:286–90.

[14] He DL, Wang YL, Wu CZ, Li Q, Ding WZ, Sun CH. Enhanced hydrogen desorption properties of magnesium hydride by coupling non-metal doping and nano-confinement. Appl Phys Lett 2015;107:243907.

[15] Norberg NS, Arthur TS, Fredrick SJ, Prieto AL. Size-dependent hydrogen storage properties of Mg nanocrystals prepared from solution. J Am Chem Soc 2011;133:10679–81.

[16] Ouyang LZ, Yang XS, Zhu M, Liu JW, Dong HW, Sun DL, Zou J, Yao XD. Enhanced hydrogen storage kinetics and stability by synergistic effects of in situ formed $CeH_{2.73}$ and Ni in $CeH_{2.73}$-MgH2-Ni nanocomposites. J Phys Chem C 2014;118:7808–20.

[17] Nielsen TK, Bosenberg U, Gosalawit R, Dornheim M, Cerenius Y, Besenbacher F, Jensen TR. A reversible nanoconfined chemical reaction. ACS Nano 2010;4:3903–8.

[18] Liu T, Chen CG, Wang F, Li XG. Enhanced hydrogen storage properties of magnesium by the synergic catalytic effect of $TiH_{1.971}$ and $TiH_{1.5}$ nanoparticles at room temperature. J Power Sources 2014;267:69–77.

[19] Cui J, Wang H, Liu JW, Ouyang LZ, Zhang QA, Sun DL, Yao XD, Zhu M. Remarkable enhancement in dehydrogenation of MgH_2 by a nano-coating of multi-valence Ti-based catalysts. J Mater Chem A 2013;1:5603–11.

[20] Hudson MSL, Takahashi K, Ramesh A, Awasthi S, Ghosh AK, Ravindrana P, Srivastava ON. Graphene decorated with Fe nanoclusters for improving the hydrogen sorption kinetics of MgH_2–experimental and theoretical evidence. Catal Sci Technol 2016;6:261–8.

[21] Liu G, Wang YJ, Jiao LF, Yuan HT. Understanding the role of few-layer graphene nanosheets in enhancing the hydrogen sorption kinetics of magnesium hydride. ACS Appl Mater Interfaces 2014;6:11038–46.

[22] Liang G, Huot J, Boily S, Van Neste A, Schulz R. Catalytic effect of transition metals on hydrogen sorption in nanocrystalline ball milled MgH_2–Tm (Tm=Ti, V, Mn, Fe and Ni) systems. J Alloy Comp 1999;292:247–52.

[23] Hanada N, Ichikawa T, Fujii H. Catalytic effect of nanoparticle 3d-transition metals on hydrogen storage properties in magnesium hydride MgH_2 prepared by mechanical milling. J Phys Chem B 2005;109:7188–94.

[24] Galey B, Auroux A, Sabo-Etienne S, Grellier M, Postole G. Enhancing hydrogen storage properties of the Mg/MgH_2 system by the addition of bis(tricyclohexylphosphine) nickel(II) dichloride. Int J Hydrogen Energy 2019;44:11939–52.

[25] Ismail M, Mustafa NS, Ali NA, Sazelee NA, Yahya MS. The hydrogen storage properties and catalytic mechanism of the $CuFe_2O_4$-doped MgH_2 composite system. Int J Hydrogen Energy 2019;44:318–24.

[26] Liu M, Xiao X, Zhao S, Yarahmadi SS, Chen M, Zheng J, Li S, Chen L. ZIF-67 derived Co@CNTs nanoparticles: remarkably improved hydrogen storage properties of MgH_2 and synergetic catalysis mechanism. Int J Hydrogen Energy 2019;44:1059–69.

[27] Yahya MS, Ismail M. Synergistic catalytic effect of $SrTiO_3$ and Ni on the hydrogen storage properties of MgH_2. Int J Hydrogen Energy 2018;43:6244–55.

[28] Zhang Q, Zang L, Huang Y, Gao P, Jiao L, Yuan H, Wang Y. Improved hydrogen storage properties of MgH2 with Ni-based compounds. Int J Hydrogen Energy 2017;42:24247–55.

[29] Lotoskyy M, Denys R, Yartys VA, Eriksen J, Goh J, Nyamsi SN, Sita C, Cummings F. An outstanding effect of graphite in nano-MgH_2–TiH_2 on hydrogen storage performance. J Mater Chem A 2018;6:10740–54.

[30] Zhang L, Chen L, Xiao X, Fan X, Shao J, Li S, Ge H, Wang Q. Fluorographene nanosheets enhanced hydrogen absorption and desorption performances of magnesium hydride. Int J Hydrogen Energy 2014;39:12715–26.

[31] Wang H, Lin HJ, Cai WT, Ouyang LZ, Zhu M. Tuning kinetics and thermodynamics of hydrogen storage in light metal

element based systems–A review of recent progress. J Alloy Comp 2016;658:280–300.
[32] Liu G, Wang Y, Qiu F, Li L, Jiao L, Yuan H. Synthesis of porous Ni@rGO nanocomposite and its synergetic effect on hydrogen sorption properties of MgH_2. J Mater Chem 2012;22:22542–9.
[33] Wang Y, Liu G, An C, Li L, Qiu F, Wang Y, Jiao L, Yuan H. Bimetallic NiCo functional graphene: an efficient catalyst for hydrogen-storage properties of MgH_2. Chem Asian J 2014;9:2576–83.
[34] Singh S, Tripathi P, Bhatnagar A, Patel CRP, Singh AP, Dhawan SK, Gupta BK, Srivastava ON. A highly porous, light weight 3D sponge like graphene aerogel for electromagnetic interference shielding applications. RSC Adv 2015;5:107083–7.
[35] Awasthi K, Kumar R, Raghuwanshi H, Awasthi S, Pandey R, Singh D, Yadav TP, Srivastava ON. Synthesis of nano-carbon (nanotubes, nanofibres, graphene) materials. Bull Mater Sci 2011;34:607–14.
[36] Sadhasivam T, Hudson MSL, Pandey SK, Bhatnagar A, Singh MK, Gurunathan K, Srivastava ON. Effects of nano size mischmetal and its oxide on improving the hydrogen sorption behaviour of MgH_2. Int J Hydrogen Energy 2013;18:7353–62.
[37] Toneguzzo P, Viau G, Acher O. CoNi and FeCoNi fine particles prepared by the polyol process: physico-chemical characterization and dynamic magnetic properties. J Mater Sci 2000;35:3767–84.
[38] Xie Z, Zhu W, Zhu B, Xia C. $Fe_xCo_{0.5-x}Ni_{0.5}$–SDC anodes for low-temperature solid oxide fuel cells. Electrochim Acta 2006;51:3052–7.
[39] Li X, Takahashi S. Synthesis and magnetic properties of Fe–Co–Ni nanoparticles by hydrogen plasma–metal reaction. J Magn Magn Mater 2000;214:195–203.
[40] Monshi A, Foroughi MR, Monshi MR. Modified scherrer equation to estimate more accurately nano-crystallite size using XRD. J Nano Sci Eng 2012;2:154–60.
[41] Saha S, Ganguli AK. FeCoNi alloy as noble metal-free electrocatalyst for oxygen evolution reaction (OER). Chem Sel 2017;2:1630–6.
[42] Sun G, Wu H, Liao Q, Zhang Y. Enhanced microwave absorption performance of highly dispersed CoNi nanostructures arrayed on graphene. Nano Res 2018;5:2689–704.
[43] Gu J, Zhang X, Fu L, Pang A. Study on the hydrogen storage properties of the dual active metals Ni and Al doped graphene composites. Int J Hydrogen Energy 2019;44(12):6036–44.
[44] Srivastava N, Shripathi T, Srivastava PC. Core level X-ray photoelectron spectroscopy study of exchange coupled Fe/NiO bilayer interfaced with Si substrate (Fe/NiO–nSi structure). J Electron Spectrosc Relat Phenom 2013;191:20–6.
[45] Yamashita T, Hayes P. Analysis of XPS spectra of Fe2+ and Fe3+ ions in oxide materials. Appl Surf Sci 2008;254:2441–9.
[46] Zhang Y, Xiao Q, Guo X, Zhang X, Xue Y, Jing L, Zhai X, Yan YM, Sun K. A novel electrocatalyst for oxygen evolution reaction based on rational anchoring of cobalt carbonate hydroxide hydrate on multiwall carbon nanotubes. J Power Sources 2015;278:464–72.
[47] Han Y, Axnanda S, Crumlin EJ, Chang R, Mao B, Hussain Z, Ross PN, Li Y, Liu Z. Observing the electrochemical oxidation of Co metal at the solid/liquid interface using ambient pressure X-ray photoelectron spectroscopy. J Phys Chem B 2018;122:666–71.
[48] Shi C, Chen M, Han X, Bi Y, Huang L, Zhou K, Zheng Z. Thiacalix[4]arene-supported tetradecanuclear cobalt nanocage cluster as precursor to synthesize CoO/Co_9S_8@CN composite for supercapacitor application. Inorg Chem Front 2018;5:1329–35.
[49] Elsener B, Atzei D, Krolikowski A, Rossi A. Effect of phosphorus concentration on the electronic structure of nanocrystalline electrodeposited Ni–P alloys: an XPS and XAES investigation. Surf Interface Anal 2008;40:919–26.
[50] Li HB, Yu MH, Wang FX, Liu P, Liang Y, Xiao J, Wang CX, Tong Y, Yang W XG. Amorphous nickel hydroxide nanospheres with ultrahigh capacitance and energy density as electrochemical pseudocapacitor materials. Nat Commun 2013;4:1894.
[51] Desimoni E, Brunetti B. X-ray photoelectron spectroscopic characterization of chemically modified electrodes used as chemical sensors and biosensors: a review. Chemosensors 2015;3:70–117.
[52] Kissinger HE. Reaction kinetics in differential thermal analysis. Anal Chem 1957;29:1702–6.
[53] Hao S, Sholl DS. Effect of TiH_2-induced strain on thermodynamics of hydrogen release from MgH_2. J Phys Chem C 2012;116:2045–50.
[54] Noritake T, Aoki M, Towata S, Seno Y, Hirose Y. Charge density analysis in magnesium hydride R & D. R D Rev Toyota CRDL 2003;38:15.
[55] Khatabi MEI, Naji S, Bhihi M, Benyoussef A, Kenza AEI, Loulidi M. Effects of double substitution on MgH2 hydrogen storage properties: an Ab initio study. J Alloy Comp 2018;743:666–71.
[56] Ri SI, Jin-Um K, Wi JH, Kim JC, Kim NH. Effects of single– and co– substitution of Ti and Fe on vacancy formation and dehydrogenation from MgH_2 (110) surface: ab initio study. Int J Hydrogen Energy 2019;44:22761–9.
[57] Yang WN, Shang CX, Guo ZX. Site density effect of Ni particles on hydrogen desorption of MgH_2. Int J Hydrogen Energy 2010;35:4534–42.
[58] Walker GS, Abbas M, Grant DM, Udeh C. Destabilisation of magnesium hydride by germanium as a new potential multi component hydrogen storage system. Chem Commun 2011;47:8001–3.
[59] Wu Z, Allendorf MD, Grossman JC. Quantum Monte Carlo simulation of nanoscale MgH_2 cluster thermodynamics. J Am Chem Soc 2009;131:13918–9.
[60] Shevlin SA, Guo ZX. MgH_2 dehydrogenation thermodynamics: nano structuring and transition metal doping. J Phys Chem C 2013;1172:110883–91.
[61] Khatabi MEI, Bhihi M, Naji S, Labrim H, Benyoussef A, Kenz AEI, Loulidi M. Study of doping effects with 3d and 4d-transition metals on the hydrogen storage properties of MgH_2. Int J Hydrogen Energy 2016;41:4712–8.
[62] Larsson P, Moyse's C, jo Arau', Larsson JA, Jena P, Ahuja R. Role of catalysts in dehydrogenation of MgH_2 nanoclusters. Proc Natl Acad Sci 2008;105:8227–31.
[63] Gong X, Shao X. Stability, electronic structure, and dehydrogenation properties of pristine and doped 2D MgH_2 by the first principles study. Metals 2018;8:482.
[64] Jiang J, Zhang C, Ai L. Hierarchical iron nickel oxide architectures derived from metal-organic frameworks as efficient electrocatalysts for oxygen evolution reaction. Electrochim Acta 2016;208:17–24.